Chemical Science

EDGE ARTICLE

View Article Online
View Journal | View Issue

Cite this: *Chem. Sci.*, 2017, **8**, 437

Achievement of visible-light-driven Z-scheme overall water splitting using barium-modified Ta_3N_5 as a H_2-evolving photocatalyst†

Yu Qi,[ab] Shanshan Chen,[a] Mingrun Li,[a] Qian Ding,[ab] Zheng Li,[ab] Junyan Cui,[ac] Beibei Dong,[ab] Fuxiang Zhang*[a] and Can Li*[a]

Received 22nd June 2016
Accepted 18th August 2016

DOI: 10.1039/c6sc02750d

www.rsc.org/chemicalscience

Ta_3N_5 is one of the most promising photocatalyst candidates for solar water splitting, but it still remains challenging to achieve overall water splitting *via* Ta_3N_5-based photocatalysts regardless of whether it uses a one step or two step method. Here we will address the relatively poor photocatalytic proton reduction of Ta_3N_5 with an effort for the promotion of charge separation *via* barium modification. One-pot nitridation of barium nitrate-impregnated Ta_2O_5 precursor was adopted here for the synthesis of Ta_3N_5 accompanied with the creation of a Ta_3N_5/$BaTaO_2N$ heterostructure and surface passivation. Due to the synergetic effect of the improved interfacial charge separation and the decreased defect density, the photocatalytic H_2 evolution rate of barium-modified Ta_3N_5 is effectively promoted. Encouraged by this, a visible-light-driven Z-scheme overall water splitting system was successfully constructed by using the barium-modified Ta_3N_5 as a H_2-evolving photocatalyst, together with a PtO_x/WO_3 and IO_3^-/I^- pair as an O_2-evolving photocatalyst and a redox mediator, respectively.

Introduction

Semiconductor-based photocatalytic overall water splitting for hydrogen production is an ideal way to convert solar energy to chemical energy and has inspired extensive interest in the past few decades.[1–5] Towards this, hundreds of semiconductors have been reported for potential solar water splitting, but most of them are only active under UV light irradiation.[6–10] To achieve highly efficient solar-to-chemical energy conversion, overall water splitting on photocatalysts harvesting visible light with longer wavelength is desirable. To date, however, the number of wide visible-light-driven overall water splitting systems, regardless of whether they use a one step or two step method, is limited.[5,11–18]

Tantalum nitride (Ta_3N_5), with a theoretical solar-to-hydrogen conversion efficiency of 15.9%, is one of the most promising candidates for solar water splitting, considering its matched band edge positions (conduction band and valence band edges at *ca.* −0.4 V and +1.7 V *vs.* NHE, respectively, at pH = 0), wide visible light harvesting ability (up to 600 nm) and good photo-stability.[19–37] It was first synthesized in 1973,[38] but was not found to be active for the photocatalytic water splitting reaction until 2002.[19] Afterwards, Ta_3N_5 has been widely investigated for water splitting in terms of particulate photocatalysts[22–25] and photoanodes.[26–31]

The increasing research interest and efforts have greatly promoted the water oxidation performance of Ta_3N_5 for both particulate photocatalyst and photoanode systems. For example, Li *et al.* fabricated a 1D Ta_3N_5 nanorod photoanode to achieve a STH of 1.5%.[30] Liu *et al.* achieved Ta_3N_5 photoanode stability for hours[27] and obtained nearly close to the theoretical photocurrent at a potential of 1.23 V *vs.* RHE under AM 1.5G simulated sunlight.[31] Chen *et al.* reported that the apparent quantum efficiency of the photocatalytic water oxidation activity of the Ta_3N_5-based particulate photocatalyst can reach 11.3% at 500–600 nm *via* an interface engineering strategy.[24] Compared to the water oxidation, however, the activity of photocatalytic proton reduction from water is much lower or even undetectable in most cases, even though extensive investigations such as forming polymorphic macroporous Ta_3N_5, reducing the particle size through templates (*i.e.* SiO_2, C_3N_4) and surface modification have been made.[32–37] As a result of the poor proton reduction ability, Z-scheme overall water splitting using particulate Ta_3N_5 as a H_2-evolving photocatalyst is still not reported.

Fabricating nanocomposites with another semiconductor to form heterostructures has been extensively adopted for the promotion of photocatalytic performances.[16,39–42] A heterostructure can create external bias through interfacial junctions to spatially separate the photogenerated electrons and holes.

[a]*State Key Laboratory of Catalysis, iChEM, Dalian Institute of Chemical Physics, Chinese Academy of Sciences, Dalian National Laboratory for Clean Energy, Dalian, 116023, China. E-mail: fxzhang@dicp.ac.cn; canli@dicp.ac.cn; Web: http://canli.dicp.ac.cn*

[b]*University of Chinese Academy of Sciences, Beijing 100049, China*

[c]*Key Laboratory of Surface and Interface Chemistry of Jilin Province, College of Chemistry, Jilin University, Changchun 130021, China*

† Electronic supplementary information (ESI) available. See DOI: 10.1039/c6sc02750d

However, it should be pointed out that most of the (oxy)nitride photocatalysts are thermally instable in air, so the fabrication of a heterostructure for (oxy)nitride commonly confronts technical challenges, rendering feasible examples very limited.[16]

In this work, a barium modification strategy is introduced to address the relatively poor photocatalytic proton reduction activity of Ta_3N_5 under visible light irradiation. A simple one-pot nitridation route was adopted for the synthesis of pristine Ta_3N_5 and barium-modified Ta_3N_5, in which a barium nitrate-impregnated Ta_2O_5 was used as a precursor. It is found that some Ba^{2+} ions could be doped into Ta_3N_5 to decrease its defect density. On the other hand, excessive Ba^{2+} ions will produce $BaTaO_2N$ *in situ* on the surface of Ta_3N_5 to create a Ta_3N_5/$BaTaO_2N$ heterostructure. As a result, the photogenerated carrier separation efficiency of Ta_3N_5 can be promoted after the barium modification, causing an effectively enhanced H_2 evolution rate in the presence of methanol. Finally, the first example of a visible-light-driven photocatalytic Z-scheme overall water splitting system using the modified Ta_3N_5 as a H_2-evolving photocatalyst was successfully constructed.

Experimental

Materials and reagents

For the preparation of Ba(n)-Ta_3N_5 samples, Ta_2O_5 (99.99%, Amresco Chemical), and $Ba(NO_3)_2$ (99.5%, Sinopharm Chemical) were used. WO_3 (99.99%, High Purity Chemical) was used as a water oxidation photocatalyst. $H_2PtCl_6{\cdot}6H_2O$ (99.5%, Sinopharm Chemical) was employed as the precursor for the reduction cocatalyst. CH_3OH (99.5%, Sinopharm Chemical) and NaI (99.5%, Guangfu Chemical) were used as sacrificial electron donors. La_2O_3 (99.95%, Sinopharm Chemical) was applied as a pH buffer agent. All chemicals were used as purchased without further purification.

Preparation of Ba(n)–Ta_3N_5 samples

Typically, Ta_2O_5 powder was impregnated in the $Ba(NO_3)_2$ aqueous solution with a calculated molar ratio of Ba/Ta, and the dried mixture was then annealed in air at 1073 K for 2 h. The as-prepared powder was treated with "one-pot" nitridation under ammonia flow (250 mL min^{-1}) at 1223 K for 20 h. The as-obtained samples are correspondingly denoted as Ba(n)–Ta_3N_5, where "n" stands for the molar ratio of Ba/Ta and when $n = 1$ it stands for $BaTaO_2N$. As a comparison, the pure phase of Ta_3N_5 and $BaTaO_2N$ powder was mechanically mixed at a Ba/Ta molar ratio of 0.3, which is denoted as Ta_3N_5/$BaTaO_2N$ (0.3)-mix.

Deposition of cocatalysts

0.2 g of the as-obtained sample was dispersed in a calculated amount of H_2PtCl_6 aqueous solution, and sonicated for *ca.* 5 min. After the solution was completely evaporated in a water bath at 353 K, the resulting powder was collected and reduced at 473 K for 1 h under a flow of 5% H_2/Ar (200 mL min^{-1}). As for the deposition of PtO_x on the surface of WO_3 for water oxidation, typically, 0.3 g of WO_3 was annealed in the air at 773 K for 2 h, and then 0.2 g of the annealed sample was immersed in a calculated amount of H_2PtCl_6 aqueous solution with sonicating for *ca.* 5 min. After complete evaporation in a water bath at 353 K, the resulting powder was collected and annealed in air at 798 K for 0.5 h.

Electrochemical analysis

For the Mott–Schottky (M–S) measurement, Ta_3N_5 and $BaTaO_2N$ powder were deposited on FTO conducting glass *via* electrophoretic deposition (EPD). Typically, the powder samples (50 mg) and iodine (20 mg) were dispersed in acetone solution (50 mL), and continuously sonicated for 10 min. Afterwards, the FTO electrode was immersed, parallel to another FTO electrode, with a distance of about 1 cm. The duration time was 1 min with 20 V and 1 A applied using a potentiostat (ITECH IT6834), and then the prepared electrodes were calcined under an ammonia flow (250 mL min^{-1}) at 723 K for 0.5 h.

The M–S measurement was carried out using a Princeton Applied Research PARSTAT 2273, using 0.5 M Na_2SO_4 aqueous solution as electrolyte with a pH value of 8.5 adjusted using NaOH. The frequency was 1 kHz.

Characterizations of catalysts

XRD measurements were carried out using a Rigaku D/Max-2500/PC powder diffractometer (Cu Kα radiation) with an operating voltage of 40 kV and an operating current of 200 mA. A scan rate of 5° min^{-1} was applied in the range of 10–60°. UV-vis diffuse reflectance spectra (DRS) were recorded using a UV-vis spectrophotometer (JASCO V-550) equipped with an integrating sphere, and $BaSO_4$ powder was used as the reference for the baseline correction. The morphologies and particle sizes were examined using field emission scanning electron microscopy (FESEM; S-5500, Hitachi). High-resolution transmission electron microscopy (HRTEM) images were obtained using a Tecnai G2 F30 S-Twin (FEI Company) with an accelerating voltage of 300 kV. For the time-resolved IR spectroscopic study, the photocatalyst was fixed on a CaF_2 plate at a density of 2 mg cm^{-2} and placed in a gas cell evacuated at 10^{-5} Torr. The Brunauer–Emmett–Teller (BET) surface area was measured at 77 K using a Micromeritics ASAP 2000 adsorption analyzer. Transient IR absorption signals were recorded on a Nicolet 870 FTIR spectrometer with a MCT detector. A pulse laser at 355 nm (1 Hz, 3 mJ per pulse) was used to excite the samples. The width of the laser pulse was 6–8 ns and no deconvolution on the data was carried out.

Photocatalytic reactions

Photocatalytic reactions were carried out in a Pyrex top-irradiation type reaction vessel connected to a closed gas circulation system. Before photoirradiation, the reaction system was evacuated to completely remove air, and then irradiated from the top side using a 300 W xenon lamp with a filtration mirror equipped with an optical filter (Hoya, L-42; $\lambda > 420$ nm) to cut off the ultraviolet light. A flow of cooling water was used to keep the reaction suspension at room temperature. Gas chromatography (Agilent; GC-7890A, MS-5A column, TCD, Ar carrier) was used to

analyze the evolved gases. The pH value before and after the photocatalytic overall water splitting reaction was similarly kept at *ca.* 6.

Measurement of AQE

The AQE measurement was carried out using a Pyrex top-irradiation-type reaction vessel and a 300 W xenon lamp fitted with a 420 nm band-pass filter. The number of photons reaching the reaction solution was measured using a calibrated Si photodiode (LS-100, EKO Instruments Co., LTD.), and the AQE (φ) was calculated according to the following equation:

$$\varphi(\%) = (AR/I) \times 100$$

where A represents a coefficient (4 for H_2 evolution; 8 for O_2 evolution), R represents the evolution rate of H_2 or O_2 in the initial one hour irradiation and I represents the absorption rate of incident photons. It was assumed that all incident photons were absorbed by the suspension. The total number of incident photons at a wavelength of 420 nm was measured to be 4.76×10^{20} photons per h.

Results and discussion

Fig. 1A shows XRD patterns of the Ba(n)–Ta_3N_5 samples (n = 0–1), in which all of them exhibit a well-crystallized feature. When the Ba/Ta molar ratio is below 0.03, only diffraction peaks assigned to a single phase of Ta_3N_5 are observed. With a further enhanced molar ratio of Ba/Ta, additional diffraction peaks attributed to $BaTaO_2N$ appear, the intensities of which are continuously increased. Compared with the diffraction peaks of the unmodified Ta_3N_5 sample, a little shift in the diffraction peaks toward a lower angle is observed for the barium-modified Ta_3N_5 samples (Fig. S1†). This demonstrates that the six-coordinated Ba^{2+} may be partly doped into Ta_3N_5 to substitute the Ta^{5+} sites, similar to the previous report.[30]

Fig. 1B shows the UV-vis spectra of the Ba(n)–Ta_3N_5 samples, in which all of the samples similarly exhibit a wide visible light absorption at around 600 nm. The absorption edge is continuously red-shifted with the increasing molar ratio of Ba/Ta, which should be the result of the formed $BaTaO_2N$ species. Compared to the pristine Ta_3N_5 sample, the absorption background originating from the formation of reduced tantalum species (*e.g.*, Ta^{4+} and Ta^{3+})[43,44] on the Ba(n)–Ta_3N_5 samples undergoes an initial decrease and a subsequent increase with the enhancing molar ratio of Ba/Ta. To understand the UV-Vis results, a single phase of $BaTaO_2N$ was prepared *via* the same preparation procedure. As shown in Fig. 1B, the absorption edge of $BaTaO_2N$ is at about 660 nm, and its absorption background is the highest among all of the Ta_3N_5-based samples. It is generally understood that the UV-vis absorption background of the mechanically mixed sample containing two phases should be located between that of the corresponding single phases. That is to say, if the Ba(n)–Ta_3N_5 samples are just a simple mixture of Ta_3N_5 and $BaTaO_2N$, the absorption background of the Ba(n)–Ta_3N_5 samples will lie between those of the Ta_3N_5 and $BaTaO_2N$. In this work, however, the samples with

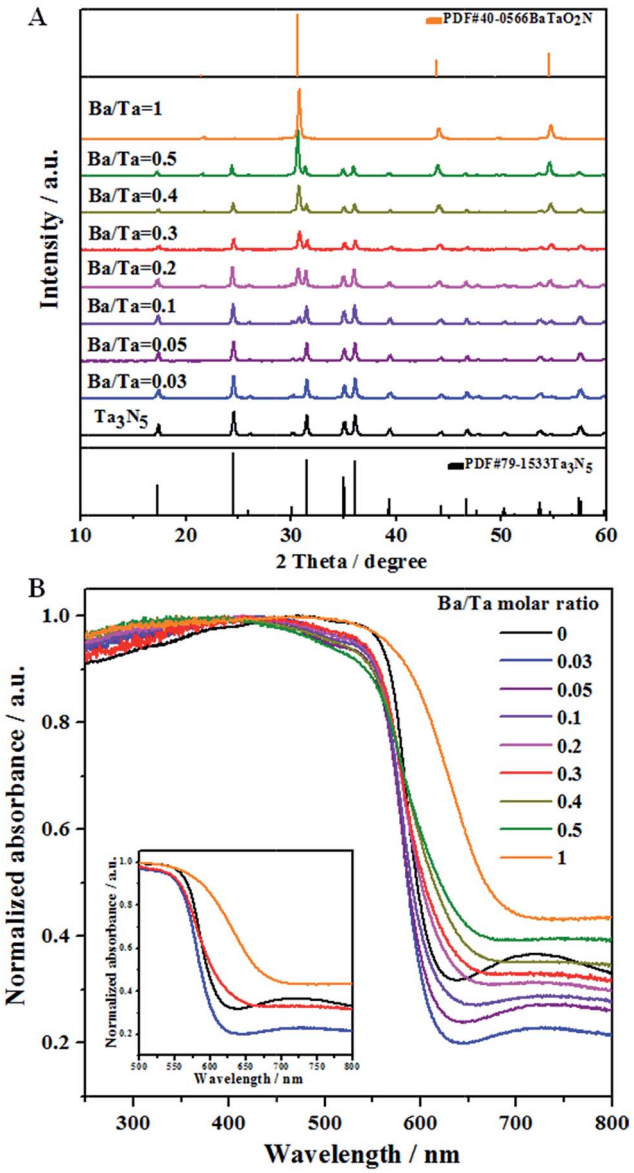

Fig. 1 Structural characterizations of typical Ba(n)–Ta_3N_5 samples (n = 0–1): (A) XRD patterns and (B) UV-vis spectra. "n" stands for the molar ratio of Ba/Ta. The inset figure is enlarged for the wavelength range of 500–800 nm.

a molar ratio of Ba/Ta below 0.3 exhibit much lower absorption backgrounds than those of both Ta_3N_5 and $BaTaO_2N$. This means that the as obtained Ba(n)–Ta_3N_5 samples do not exist as a simple mixture of Ta_3N_5 and $BaTaO_2N$, but exist as a nanocomposite. In consideration of that, here the Ta_3N_5 and $BaTaO_2N$ phases are one-pot synthesized, thus the $BaTaO_2N$ is expected to be formed *in situ* on the surface of Ta_3N_5 to partly eliminate the surface dangling bonds of Ta_3N_5. On the other hand, the partial barium ions are doped into Ta_3N_5 to inhibit the defect formation. Both of them cause the decrease of defect density. However, it needs to be pointed out that $BaTaO_2N$ itself exhibits the highest defect density among all of the samples. Thus, when the molar ratio of Ba/Ta is excessively enhanced, the defect density of the Ba(n)–Ta_3N_5 sample will become higher

than that of Ta_3N_5. All of these factors should be integrally responsible for the initial decrease and subsequent increase of the absorption background (*i.e.* defect density) with the increasing molar ratio of Ba/Ta in the UV-Vis results (Fig. 1B).

Fig. 2 shows FESEM images of typical samples. The Ta_3N_5 sample is porous (Fig. 2a), while the $BaTaO_2N$ sample has a shortage of porosity (Fig. 2b). The difference in their morphology can be easily judged from their mixed sample (Fig. 2c). However, the morphology feature of the chosen Ba(0.3)–Ta_3N_5 sample (Fig. 2d) prepared in this work is quite different from those of the corresponding single phases (Fig. 2a and b) or their mixed sample (Fig. 2c). As can be seen in Fig. 2d, the Ba(0.3)–Ta_3N_5 sample exhibits a homogeneous morphology with the two phases difficult to distinguish, demonstrating their interaction with each other as a nanocomposite. The formation of the Ta_3N_5/$BaTaO_2N$ nanocomposite can be further supported by the elemental mapping results (Fig. 2e–h). In Fig. 2f, the Ta element originating from both Ta_3N_5 and $BaTaO_2N$ is dispersed everywhere, while the Ba element that can only result from $BaTaO_2N$ is only found in some specific places (Fig. 2g). This can be easily understood to show that the places with Ba element mapping mainly reveal the existence of $BaTaO_2N$, while the locations with Ta element mapping but a shortage of Ba element mapping stand for the Ta_3N_5 species. Based on the elemental mapping images, we can reasonably give a simulation of the composite state of Ta_3N_5 and $BaTaO_2N$ for the Ba(0.3)–Ta_3N_5 sample (Fig. 2h). For comparison, the element mapping results of mechanically mixed Ta_3N_5 and $BaTaO_2N$ (Ta_3N_5/$BaTaO_2N$ (0.3)-mix) are given in Fig. S2,† from which the Ta_3N_5 and $BaTaO_2N$ phases are mainly separated, different from that of the Ba(0.3)–Ta_3N_5 sample. It needs to be pointed out that the composite of Ta_3N_5 and $BaTaO_2N$ does not exist in a core–shell configuration. In addition, the surface areas of the Ba(*n*)–Ta_3N_5 samples are similar to that of $BaTaO_2N$ (7 m^2 g^{-1}) but a little lower than that of Ta_3N_5 (9 m^2 g^{-1}), which should result from their shortage of porous structure (Table 1).

To further confirm the formation of the nanocomposite, we carried out a (HR)TEM characterization. Fig. 3 gives the representative images of the Ba(0.3)–Ta_3N_5 sample, in which the interface of the nanocomposite can be clearly observed. As shown in Fig. 3, the obvious lattice fringes indicate that the sample synthesized in this work is well-crystallized, in accordance with the XRD patterns (Fig. 1A). Based on the measurement of lattice distance, we can easily judge the $BaTaO_2N$ and Ta_3N_5 phases. Strikingly, the interfacial contact between $BaTaO_2N$ and Ta_3N_5 is very intimate, revealing the formation of the nanocomposite. The formation of the intimate interface should originate from the one-pot high temperature route and their similar Ta-based octahedron units. In this case, $BaTaO_2N$ is expected to be formed *in situ* on the surface of Ta_3N_5 during the one-pot nitridation process.

The relative band positions of Ta_3N_5 and $BaTaO_2N$ were analysed by combining their Mott–Schottky (M–S) plots and UV-Vis results. In Fig. 4a, the flat band potentials of $BaTaO_2N$ and Ta_3N_5 were evaluated according to M–S measurement results to be *ca.* −0.41 V and −0.32 V *vs.* NHE, respectively. In consideration of the fact that the bottom of the conduction band (CB) for one n-type semiconductor is normally more negative by *ca.* 0.2 V than the flat band potential,[24,45,46] the CB positions of the n-type Ta_3N_5 and $BaTaO_2N$ are estimated to be −0.52 eV and −0.61 eV, respectively. By combining their bandgaps achieved from the UV-Vis results (Fig. 1B), the relative band positions of $BaTaO_2N$ and Ta_3N_5 are then deduced and given in Fig. 4b. Accordingly, the nanocomposite exists as a type II heterostructure, where the excited electrons are expected to transfer from the conduction band of $BaTaO_2N$ to that of Ta_3N_5, while the photogenerated holes will transfer in an opposite way, leading to the spatial charge separation.

The photocatalytic H_2 evolution rates on the pristine and modified Ta_3N_5 samples were examined using the deposited platinum nanoparticle as the reduction cocatalyst in the presence of CH_3OH under visible light irradiation (λ > 420 nm). No reaction takes place in the dark, and H_2 is evolved only under light irradiation. As given in the half reaction part of Table 1, the rate of H_2 evolution undergoes an initial increase and subsequent decrease with the increasing molar ratio of Ba/Ta, and the optimal value of the Ba/Ta molar ratio

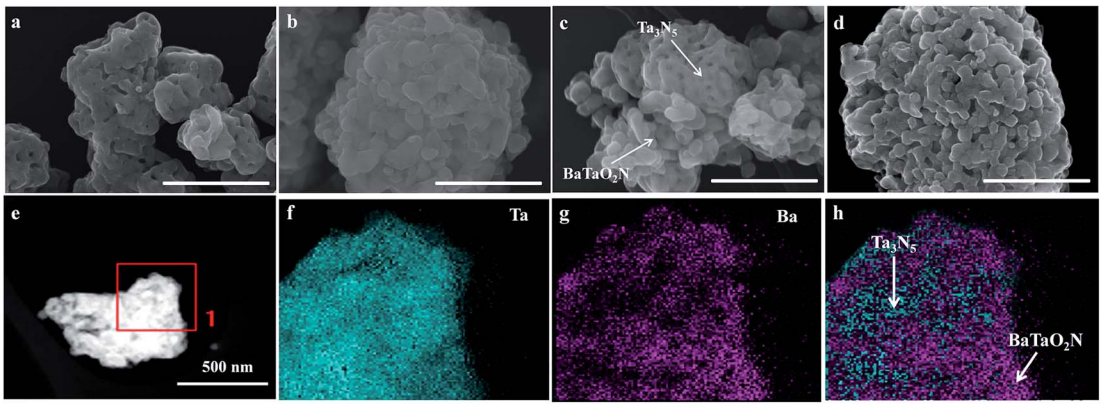

Fig. 2 FESEM images of typical samples: (a) Ta_3N_5, (b) $BaTaO_2N$, (c) a mixture of Ta_3N_5 and $BaTaO_2N$, and (d) Ba(0.3)–Ta_3N_5 (the scale bar is 500 nm). Elemental mappings of Ba(0.3)–Ta_3N_5: (e) TEM image, (f) Ta element, (g) Ba element, and (h) simulated dispersion of Ta_3N_5 and $BaTaO_2N$.

Table 1 Photocatalytic performances of typical photocatalysts under visible light irradiation ($\lambda > 420$ nm)

			Half reaction[a]	Overall water splitting[b]	
				Gas evolution rates (μmol h^{-1})	
Entry	H_2-evolving photocatalysts	Surface area (m^2 g^{-1})	H_2 evolution rate (μmol h^{-1})	H_2	O_2
1	Ba(0)–Ta_3N_5	9	0.05	0	0
2	Ba(0.03)–Ta_3N_5	7	0.1	Trace	Trace
3	Ba(0.05)–Ta_3N_5	7	4.2	0.8	0.4
4	Ba(0.1)–Ta_3N_5	7	6.6	2.0	1.0
5	Ba(0.2)–Ta_3N_5	7	19.3	2.5	1.3
6	Ba(0.3)–Ta_3N_5	7	30.2	3.2	1.6
7	Ba(0.4)–Ta_3N_5	7	28.2	3.0	1.5
8	Ba(0.5)–Ta_3N_5	7	24.6	2.1	1.1
9	$BaTaO_2N$	7	9.5	0.3	0.15
10	Ta_3N_5/$BaTaO_2N$ (0.3)-mix	8	16.5	0.6	0.3

[a] Reaction conditions: 0.15 g of 0.5 wt% Pt/Ba(n)–Ta_3N_5 (n = 0–1) and 0.5 wt% Pt/Ta_3N_5/$BaTaO_2N$ (0.3)-mix samples; 0.15 g of La_2O_3; aqueous methanol solution (150 mL, 20 vol%); 300 W xenon lamp ($\lambda > 420$ nm); 1 h irradiation. [b] Reaction conditions: 50 mg of 0.5 wt% Pt-modified H_2-evolving photocatalysts; 50 mg of 0.45 wt% PtO_x/WO_3 as O_2-evolving photocatalyst; 100 mL of aqueous NaI solution (1.0 mM); Pyrex top-irradiation type; 300 W xenon lamp ($\lambda > 420$ nm); 1 h irradiation.

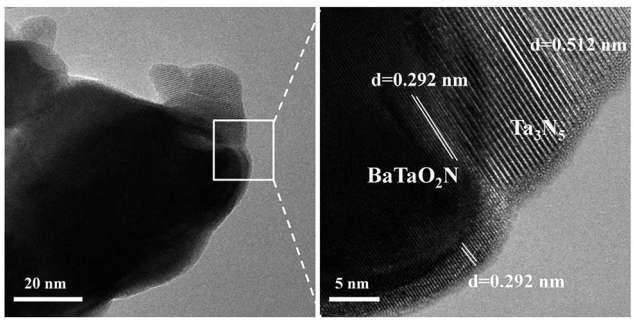

Fig. 3 Representative TEM (left) and locally enlarged HRTEM (right) images of the chosen Ba(0.3)–Ta_3N_5 sample.

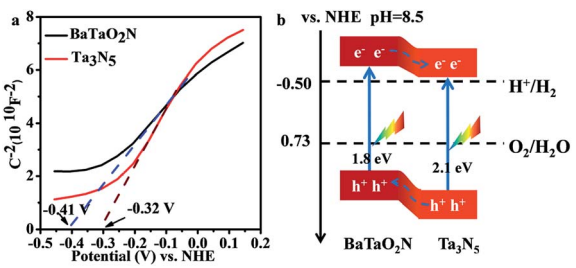

Fig. 4 Band structure characterizations of the Ta_3N_5 and $BaTaO_2N$ samples. (a) Mott–Schottky plot for the Ta_3N_5 and $BaTaO_2N$ electrodes. Electrolyte: 0.5 M Na_2SO_4 solution (pH = 8.5, adjusted using NaOH). Frequency: 1000 Hz. (b) The relative band positions of the Ta_3N_5/$BaTaO_2N$ heterostructure.

is 0.3. Compared to the Ta_3N_5 (entry 1), $BaTaO_2N$ (entry 9) or Ta_3N_5/$BaTaO_2N$ (0.3)-mix (entry 10) sample, the H_2 evolution rate on the Pt/Ba(0.3)–Ta_3N_5 photocatalyst is remarkably promoted. The typical time curve of H_2 evolution on the Pt/Ba(0.3)–Ta_3N_5 sample is given in Fig. S3,† in which it is almost linearly increased in the experimental region, demonstrating its good photochemical stability. In addition, only a small amount of N_2 (less than 1 μmol) was detected in the initial stage of irradiation. The dependence of the H_2 evolution rate on the Pt/Ba(0.3)–Ta_3N_5 photocatalyst as a function of irradiation wavelength is well consistent with that of the UV-vis spectra (Fig. S4†), indicating that the H_2 evolution process is driven by the incident light.

Encouraged by the significantly enhanced H_2 evolution rate, we tried to use the pristine or barium-modified Ta_3N_5 samples as H_2-evolving photocatalysts to construct a Z-scheme overall water splitting system together with a PtO_x/WO_3 and IO_3^-/I^- pair as an O_2-evoloving photocatalyst and redox mediator, respectively. As shown in the overall water splitting part of Table 1, when using pristine Ta_3N_5 as the H_2-evolving photocatalyst (entry 1), no obvious H_2 evolution is detected, demonstrating the infeasibility of Ta_3N_5 itself to drive the Z-scheme overall water splitting process. However, using the barium-modified Ta_3N_5 samples as H_2-evolving photocatalysts (entries 2–8), overall water splitting with H_2/O_2 molar ratios of close to 2 : 1 is achieved, and the photocatalytic activity is dependent on the Ba/Ta molar ratio with an optimal value of *ca.* 0.3. The Z-scheme activities using the barium-modified samples as H_2-evolving photocatalysts (entries 2–8) are all higher than those using $BaTaO_2N$ (entry 9) or the mixed sample (entry 10). The AQE was measured using the Ba(0.3)–Ta_3N_5 sample as the H_2-evolving photocatalyst to be 0.1% at 420 nm. The activity trend is similar to the result of the photocatalytic proton reduction reaction, indicating that the overall water splitting performance is rate-determined by the H_2-evolving side. In addition, the multiple cycles of time course curves further demonstrate its photochemical stability in the experimental region (Fig. 5). No obvious Ba^{2+} ion residue is observed in the centrifuged solution after reaction.

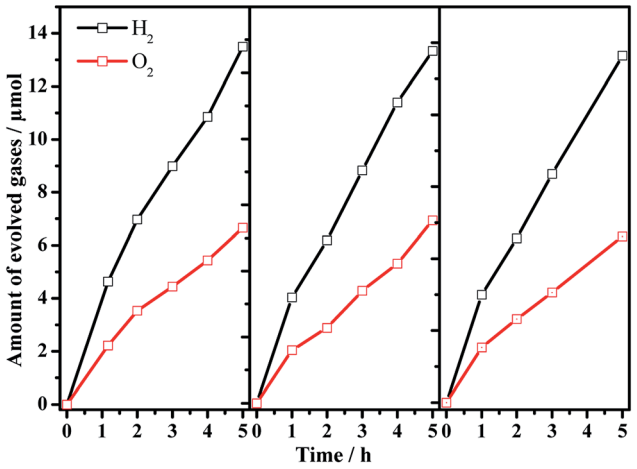

Fig. 5 Multiple cycles of Z-scheme overall water splitting with 0.5 wt% Pt/Ba(0.3)–Ta_3N_5 and 0.45 wt% PtO_x/WO_3 as H_2-evolving and O_2-evolving photocatalysts, respectively. Reaction conditions: 50 mg of Pt/Ba(0.3)–Ta_3N_5 and 50 mg of PtO_x/WO_3; 100 mL of NaI aqueous solution (1.0 mM); 300 W xenon lamp ($\lambda > 420$ nm), top-irradiation.

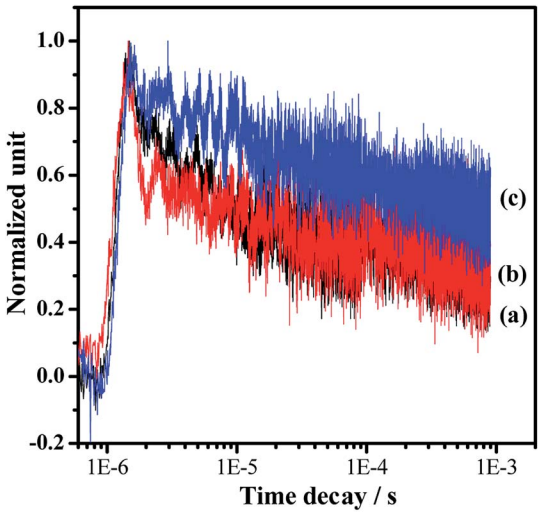

Fig. 6 Normalized transient absorption profiles of the representative samples in a vacuum: (a) Pt/Ta_3N_5, (b) Pt/$BaTaO_2N$ and (c) Pt/Ba(0.3)–Ta_3N_5. The pulse laser at 355 nm was used to excite the samples for the IR tests. The cocatalyst of Pt with a loading amount of 0.5 wt% was deposited by impregnation and a subsequent H_2 reduction method.

Photocatalytic overall water splitting commonly confronts huge challenges from both thermodynamic and kinetic aspects.[2,47] In the past few decades, many candidate materials have satisfied the thermodynamics requirement, but overall water splitting on them is unfeasible because of the constraint of insufficient reaction kinetics in the H_2 and/or O_2-evolving side. Accordingly, developing strategies to address the water splitting reaction kinetics, which is greatly affected by the charge separation and surface catalytic process, is highly valuable. In this work, we adopt a simple one-pot nitridation approach with an ammonia flow (250 mL min^{-1}) at high temperature (1223 K) to address the key issue of the charge separation *via* barium modification of Ta_3N_5. Based on our modification, not only is the defect density of Ta_3N_5 decreased, but also a $Ta_3N_5/BaTaO_2N$ heterostructure with intimate interfacial contact is formed for the promotion of spatial charge separation. Both of these are reasonably responsible for promoting photogenerated charge separation, contributing to the enhanced proton reduction performance as well as the feasible overall water splitting process. The promotion of charge separation is confirmed by comparing the time-resolved infrared spectra (TRIR) of the typical Ta_3N_5, $BaTaO_2N$ and Ba(0.3)–Ta_3N_5 samples (Fig. 6). The effective formation of the $Ta_3N_5/BaTaO_2N$ heterostructure probably originates from their similar structure units containing Ta-based octahedra. The decreased defect density of Ta_3N_5 originates from the part doping of Ba ions and the formation of $BaTaO_2N$ on the surface of Ta_3N_5 leading to surface passivation. It needs to be pointed out that with the increasing Ba/Ta molar ratio, the content of $BaTaO_2N$ with the highest defect density (see UV-Vis results in Fig. 1B) is enhanced, resulting in the increase of recombination centres, which is unfavourable for the photocatalytic H_2 evolution process. As an integral factor of the heterostructure and the defect centres, the photocatalytic activity exhibits an initial increase and a subsequent decrease with the increasing molar ratio of Ba/Ta.

Conclusions

In summary, a simple one-pot nitridation strategy is adopted for the barium modification of Ta_3N_5 photocatalyst to address its poor photogenerated carrier separation ability as well as H_2-evolving activity. The one-pot nitridation route overcomes well the challenge of low thermal stability in air for (oxy)nitride-related photocatalysts. Based on this, barium ions are partially doped into Ta_3N_5 to inhibit the formation of defects, and the residue amount of barium ions will cause the *in situ* formation of $BaTaO_2N$ on the surface of Ta_3N_5 to create an intimate interface for the $Ta_3N_5/BaTaO_2N$ heterostructure. Both of the structures favour the enhancement of charge separation efficiency as well as the promotion of the H_2-evolving rate. Finally, we successfully achieve a Z-scheme overall water splitting process under visible light irradiation using the Ba-modified Ta_3N_5 as a H_2-evolving photocatalyst. The fabrication of the heterostructure *via* a one-pot route is expected to be extended into more (oxy)nitride systems for promoted solar energy conversion.

Acknowledgements

This work was financially supported by the Basic Research Program of China (973 Program: 2014CB239403) and National Natural Science Foundation of China (21373210, 21522306). F. Zhang thanks the "Hundred Talents Program" of Chinese Academy of Sciences for the preferential support.

Notes and references

1 K. Maeda and K. Domen, *J. Phys. Chem. C*, 2007, **111**, 7851–7861.
2 A. Kudo and Y. Miseki, *Chem. Soc. Rev.*, 2009, **38**, 253–278.

3 R. Abe, *J. Photochem. Photobiol., C*, 2010, **11**, 179–209.
4 X. Zong and L. Z. Wang, *J. Photochem. Photobiol., C*, 2014, **18**, 32–49.
5 D. M. Fabian, S. Hu, N. Singh, F. A. Houle, T. Hisatomi, K. Domen, F. E. Osterloh and S. Ardo, *Energy Environ. Sci.*, 2015, **8**, 2825–2850.
6 F. E. Osterloh, *Chem. Mater.*, 2008, **20**, 35–54.
7 H. Tong, S. X. Ouyang, Y. P. Bi, N. Umezawa, M. Oshikiri and J. H. Ye, *Adv. Mater.*, 2012, **24**, 229–251.
8 X. B. Chen, S. H. Shen, L. J. Guo and S. S. Mao, *Chem. Rev.*, 2010, **110**, 6503–6570.
9 Y. Wang, X. C. Wang and M. Antonietti, *Angew. Chem., Int. Ed.*, 2012, **51**, 68–89.
10 Y. Ma, X. L. Wang, Y. S. Jia, X. B. Chen, H. X. Han and C. Li, *Chem. Rev.*, 2014, **114**, 9987–10043.
11 K. Maeda, K. Teramura, D. L. Lu, T. Takata, N. Saito, Y. Inoue and K. Domen, *Nature*, 2006, **440**, 295.
12 Y. Sasaki, H. Kato and A. Kudo, *J. Am. Chem. Soc.*, 2013, **135**, 5441–5449.
13 W. Y. Wang, J. Chen, C. Li and W. M. Tian, *Nat. Commun.*, 2014, **5**, 4647.
14 C. S. Pan, T. Takata, M. Nakabayashi, T. Matsumoto, N. Shibata, Y. Ikuhara and K. Domen, *Angew. Chem., Int. Ed.*, 2015, **54**, 2955–2959.
15 Q. X. Jia, A. Iwase and A. Kudo, *Chem. Sci.*, 2014, **5**, 1513–1519.
16 S. S. Chen, Y. Qi, T. Hisatomi, Q. Ding, T. Asai, Z. Li, S. S. K. Ma, F. X. Zhang, K. Domen and C. Li, *Angew. Chem., Int. Ed.*, 2015, **54**, 8498–8501.
17 D. J. Martin, P. J. T. Reardon, S. J. A. Moniz and J. W. Tang, *J. Am. Chem. Soc.*, 2014, **136**, 12568–12571.
18 G. G. Zhang, Z. A. Lan, L. H. Lin, S. Lin and X. C. Wang, *Chem. Sci.*, 2016, **7**, 3062–3066.
19 G. Hitoki, A. Ishikawa, T. Takata, J. N. Kondo, M. Hara and K. Domen, *Chem. Lett.*, 2002, 736–737.
20 A. Ishikawa, T. Takata, J. N. Kondo, M. Hara and K. Domen, *J. Phys. Chem. B*, 2004, **108**, 11049–11053.
21 A. B. Murphy, P. R. F. Barnes, L. K. Randeniya, I. C. Plumb, I. E. Grey, M. D. Horne and J. A. Glasscock, *Int. J. Hydrogen Energy*, 2006, **31**, 1999–2017.
22 S. S. K. Ma, T. Hisatomi, K. Maeda, Y. Moriya and K. Domen, *J.Am. Chem. Soc.*, 2012, **134**, 19993–19996.
23 Z. Wang, J. G. Hou, S. Q. Jiao, K. Huang and H. Zhu, *J. Mater. Chem.*, 2012, **22**, 21972–21978.
24 S. S. Chen, G. J. Liu, Y. Qi, F. X. Zhang and C. Li, *Angew. Chem., Int. Ed.*, 2015, **54**, 3047–3051.
25 M. Tabata, K. Maeda, M. Higashi, D. L. Lu, T. Takata, R. Abe and K. Domen, *Langmuir*, 2010, **26**, 9161–9165.
26 M. J. Liao, J. Y. Feng, W. J. Luo, Z. Q. Wang, J. Y. Zhang, Z. S. Li, T. Yu and Z. Z. Zou, *Adv. Funct. Mater.*, 2012, **22**, 3066–3074.
27 G. J. Liu, J. Y. Shi, F. X. Zhang, Z. Chen, J. F. Han, C. M. Ding, S. S. Chen, Z. L. Wang, H. X. Han and C. Li, *Angew. Chem., Int. Ed.*, 2014, **53**, 7295–7299.
28 L. Wang, N. T. Nguyen, X. M. Zhou, I. Hwang, M. S. Killian and P. Schmuki, *ChemSusChem*, 2015, **8**, 2615–2620.
29 J. Seo, T. Takata, M. Nakabayashi, T. Hisatomi, N. Shibata, T. Minegishi and K. Domen, *J. Am. Chem. Soc.*, 2015, **137**, 12780–12783.
30 Y. B. Li, L. Zhang, A. Torres-Pardo, J. M. Gonzalez-Calbet, Y. H. Ma, P. Oleynikov, O. Terasaki, S. Asahina, M. Shima, D. Cha, L. Zhao, K. Takanabe, J. Kubota and K. Domen, *Nat. Commun.*, 2013, **4**, 2566.
31 G. J. Liu, S. Ye, P. L. Yan, F. Q. Xiong, P. Fu, Z. L. Wang, Z. Chen, J. Y. Shi and C. Li, *Energy Environ. Sci.*, 2016, **9**, 1327–1334.
32 M. Y. Tsang, N. E. Pridmore, L. J. Gillie, Y. H. Chou, R. Brydson and R. E. Douthwaite, *Adv. Mater.*, 2012, **24**, 3406–3409.
33 L. Yuliati, J. H. Yang, X. C. Wang, K. Maeda, T. Takata, M. Antonietti and K. Domen, *J. Mater. Chem.*, 2010, **20**, 4295–4299.
34 K. Maeda, N. Nishimura and K. Domen, *Appl. Catal., A*, 2009, **370**, 88–92.
35 D. A. Wang, T. Hisatomi, T. Takata, C. S. Pan, M. Katayama, J. Kubota and K. Domen, *Angew. Chem., Int. Ed.*, 2013, **52**, 11252–11256.
36 X. M. Liu, L. Zhao, K. Domen and K. Takanabe, *Mater. Res. Bull.*, 2014, **49**, 58–65.
37 S. S. Chen, Y. Qi, Q. Ding, Z. Li, J. Y. Cui, F. X. Zhang and C. Li, *J. Catal.*, 2016, **339**, 77–83.
38 V. Strahle, *Z. Anorg. Allg. Chem.*, 1973, **402**, 47–57.
39 J. Zhang, Q. Xu, Z. C. Feng, M. J. Li and C. Li, *Angew. Chem., Int. Ed.*, 2008, **47**, 1766–1769.
40 X. Wang, Q. Xu, M. R. Li, S. Shen, X. L. Wang, Y. C. Wang, Z. C. Feng, Y. S. Shi, H. X. Han and C. Li, *Angew. Chem., Int. Ed.*, 2012, **51**, 13089–13092.
41 J. Z. Su, L. J. Cuo, N. Z. Bao and C. A. Grimes, *Nano Lett.*, 2011, **11**, 1928–1933.
42 E. S. Kim, N. Nishimura, G. Magesh, J. Y. Kim, J. W. Jang, H. Jun, J. Kubota, K. Domen and J. S. Lee, *J. Am. Chem. Soc.*, 2013, **135**, 5375–5383.
43 J. Q. Wang, S. Y. Su, B. Liu, M. H. Cao and C. W. Hu, *Chem. Commun.*, 2013, **49**, 7830–7832.
44 K. Maeda, M. Higashi, D. L. Lu, R. Abe and K. Domen, *J. Am. Chem. Soc.*, 2010, **132**, 5858–5868.
45 Y. Matsumoto, *J. Solid State Chem.*, 1996, **126**, 227–234.
46 S. S. Chen, Q. Yi, G. J. Liu, J. X. Yang, F. X. Zhang and C. Li, *Chem. Commun.*, 2014, **50**, 14415–14417.
47 T. Hisatomi, J. Kubota and K. Domen, *Chem. Soc. Rev.*, 2014, **43**, 7520–7535.